1 Using Spectral Methods to Obtain Particle Size Information from Optical Data:
2 Applications to Measurements from CARES 2010

3 Dean B. Atkinson[1], Mikhail Pekour[2], Duli Chand[2], James G. Radney[1,***], Katheryn R. Kolesar[5,*], Qi Zhang[3],

4 Ari Setyan[3,**], Norman T. O'Neill[4], Christopher D. Cappa[5]

5 [1] [Department of Chemistry, Portland State University, Portland, OR, USA, 97207]

6 [2] [Pacific Northwest National Laboratory, Richland, WA, USA, 99352]

7 [3] [Department of Environmental Toxicology, University of California, Davis, CA, USA, 95616]

8 [4] [Centre d'Applications et de Recherches en Télédétection, Université de Sherbrooke, Sherbrooke,

9 Canada]

10 [5] [Department of Civil and Environmental Engineering, University of California, Davis, CA, USA, 95616]

11 * Now at: Air Sciences, Inc., Portland, OR, 97214, USA

12 ** Now at: Empa, Swiss Federal Laboratories for Materials Science and Technology, 8600 Dübendorf,

13 Switzerland

14 *** Now at: Material Measurement Laboratory, National Institute of Standards and Technology,

15 Gaithersburg, Maryland, 20899, USA

16 Correspondence to: D. B. Atkinson (atkinsond@pdx.edu)

18 **Abstract**

19 Multi-wavelength aerosol extinction, absorption and scattering measurements made at two ground sites

20 during the 2010 Carbonaceous Aerosols and Radiative Effects Study (CARES) are analyzed using a

21 spectral deconvolution method that allows extraction of particle size-related information, including the

22 fraction of extinction produced by the fine mode particles and the effective radius of the fine mode. The

23 spectral deconvolution method is typically applied to analysis of remote sensing measurements.

24 Application to *in situ* measurements allows for comparison with more direct measurement methods and

25 validation of the retrieval approach. Here, the retrieved fine mode fraction and effective radius

26 generally compare well with other *in situ* measurements, including size distribution measurements and

27 scattering and absorption measurements made separately for PM_1 and PM_{10}, but some limitations are

28 also identified. These results indicate that for campaigns where size, composition, and multi-wavelength

29 optical property measurements are made, comparison of the results can result in closure or can identify

30 unusual circumstances. The comparison here also demonstrates that *in situ* multi-wavelength optical

31 property measurements can be used to determine information about particle size distributions in

32 situations where direct size distribution measurements are not available.

33

Introduction

34

35   Aerosols remain a substantial source of uncertainty in climate models, despite considerable progress in

36   scientific understanding of their chemical, physical and optical properties in the last few decades (IPCC,

37   2013). As greater understanding has developed in each of these areas, new complexity is also uncovered

38   and the interconnectedness of the various properties becomes even more evident. Light scattering by

39   atmospheric particles has a net cooling effect on climate that is one major offset to greenhouse gas

40   induced climate warming (Charlson et al., 2005; Bond et al., 2011). The efficiency with which the

41   atmospheric aerosol interacts with electromagnetic radiation (e.g. sunlight) is dependent upon the size,

42   composition, shape and morphology of the particles. These properties are not static in time, instead

43   evolving as particles are transported through the atmosphere as a result of chemical processing,

44   scavenging and changes in the environmental conditions (e.g. relative humidity and temperature)

45   (Doran et al., 2007; George and Abbatt, 2010; Lack and Cappa, 2010).

46   Characterization of the spatial distribution of aerosol particle concentrations and properties is important

47   to assessing their impact on the atmospheric radiation budget through direct aerosol-radiation and

48   indirect aerosol-cloud interactions. Aerosol optical properties can be measured directly in the laboratory

49   and in the field using both in situ methods (Andrews et al., 2004; Moosmuller et al., 2009; Coen et al.,

50   2013) and remote sensing instruments/platforms, such as sunphotometers and satellites (Holben et al.,

51   1998; Anderson et al., 2005). Alternatively, aerosol optical properties can be inferred from

52   measurements of particle composition, abundance and size distributions (Atkinson et al., 2015). One

53   particular advantage of the remote sensing instruments is that they allow for characterization of

54   column-average atmospheric particle burdens and properties over a large spatial scale and are free from

55   sampling biases as the particles are characterized as they exist in the atmosphere. However, they can

56   only reliably retrieve aerosol properties under cloud-free conditions, and determination of properties

57   beyond the aerosol optical depth (such as the single scatter albedo or the aerosol size distribution)

58   typically requires a data 'inversion' process that relies on an assessment of the wavelength-dependent

59   light attenuation and scattering (Dubovik and King, 2000). *In situ* methods can allow for more detailed

60   characterization of aerosols, including the relationships between size, composition and optical

61   properties, but typically at the expense of reduced spatial coverage and with long-term measurements

62   typically restricted to the surface (Andrews et al., 2004). Given the wide-spread use of aerosol remote

63   sensing and the extensive availability of the data (in particular from ground-based sunphotometer

64   networks such as AERONET and AEROCAN (Holben et al., 1998; Bokoye et al., 2001)), continued

65   assessment and validation of the inversion methods by comparison with measurements by *in situ*

66   methods is important.

67   Multi-wavelength optical measurements can yield information about the aerosol size distribution, a

68   principle that dates back to Ångström's observation that the wavelength-dependence of light

69   attenuation by particles was weaker for larger particles (diameters of hundreds of nanometers to

70   micrometers) than for smaller particles (Ångström, 1929). One of the simplest ways of characterizing the

71   wavelength-dependence of optical measurements (whether extinction, scattering or absorption) is

72   through the Angstrom exponent. For a pair of optical measurements at different wavelengths, å

73    $= -\log(b_{x,\lambda 1}/b_{x,\lambda 2})/\log(\lambda_1/\lambda_2)$, where $b_{x,\lambda}$ is the optical coefficient at one of the wavelengths λ; for

74   scattering and extinction å typically increases as particle size decreases. The dependence of b_x on

75   wavelength can alternatively be obtained from a $\log(b_{x,\lambda})$ vs. $\log(\lambda)$ plot using two or more wavelengths;

76   if the dependence is linear, a regression would obtain the same value as the pair-wise treatment, but

77   non-linearity can be accommodated by using the continuous derivative $\alpha = -d\ln(b_{x,\lambda}) / d\ln(\lambda)$ at a

78   specified wavelength. (A list of the symbols and acronyms used in this work is provided in Appendix A.)

79   The former will be referred to here as the Ångström exponent and the latter as the spectral derivative.

80   Particle size classification schemes have been proposed (Clarke and Kapustin, 2010) and

81   supported/validated (Eck et al., 2008; Massoli et al., 2009; Cappa et al., 2016) based on the Ångström

82   exponent of extinction or scattering. When observations are made at more than two wavelengths

83   (ideally, widely spaced), further information regarding the nature of the particle size distribution can be

84   extracted. For example, an additional level of refinement of wavelength-dependent measurements of

85   aerosol optical depth (path integrated extinction) was introduced by O'Neill et al. (2005) to aid in the

86   interpretation of the data obtained by the ground-based sunphotometer networks AERONET and

87   AEROCAN. Specifically, O'Neill et al. (2003; 2005) showed that the fine mode fraction (FMF) of extinction

88   and the fine mode effective radius, $R_{eff,f}$ could be extracted directly from the multi-wavelength optical

89   depth or extinction measurements available from remote sensing. The FMF provides for an approximate

90   discrimination between what are typically naturally produced coarse mode particles (dust or sea spray)

91   and what are often anthropogenically associated fine mode particles. Thus, parameters such as the FMF

92   can provide a nominal indication of the relative contributions of natural versus anthropogenic particles

93   to the atmospheric AOD. Variations in $R_{eff,f}$ provide information on the sources of the fine mode particles

94   - as different sources yield fine mode particles with different size distributions - or the extent to which

95   particles have undergone atmospheric processing, which can change the size distribution (and chemical

96   composition) in systematic ways.

97   In the spectral curvature approach of O'Neill et al. (2003), the fine mode spectral derivatives (α_f = first

98   derivative and α_f' = second) and the FMF are first extracted from multi-wavelength extinction data using

99   a process described as Spectral Deconvolution (η was used for FMF in ibid.) The fine mode spectral

100   derivatives are then used to obtain the effective radius for the fine mode, defined by Hansen and Travis

101   (1974) as:

102
$$R_{eff,f} = \frac{\int_0^\infty R \pi R^2 \frac{dN}{dlnR} dlnR}{\int_0^\infty \pi R^2 \frac{dN}{dlnR} dlnR}$$
(1)

103   where R is the particle geometrical radius and dN/dlnR is a number weighted size distribution for which

104    $R_{eff,f}$ is the first moment (average radius) of the surface-area weighted size distribution. $R_{eff,f}$ is an

105   effective radius that characterizes, approximately, the average size of particles in the fine mode that

106   scatter solar radiation. In this work, we compare the optically obtained $R_{eff,f}$ retrievals to those

107   calculated from the observed size distributions (produced by scanning mobility particle sizers) by

108   numerically evaluating the integrals of Equation 1 to produce comparator values. A single log-

109   translatable particle size distribution (i.e., a PSD that can be translated along the log-transformed

110   particle size axis without changing the form of the distribution function) is, in many cases, a reasonable

111   representation of the size distribution of observed aerosol fine modes (O'Neill et al., 2005). In these

112   cases, the fine mode can be characterized by the single parameter $R_{eff,f}$ facilitating comparisons and

113   examination of trends in sources and/or atmospheric processing.

114   Methods such as those developed by O'Neill et al. (2003) for remote sensing measurements can also be

115   applied to *in situ* extinction measurements. Beyond adding to the utility of the *in situ* optical

116   measurements, this provides an opportunity to test the methods against other, complementary

117   measures of particle size and size-dependent scattering and extinction. For example, Atkinson et al.

118   (2010) used the approach of O'Neill et al. (2003) to analyze *in situ,* three-wavelength aerosol extinction

119   measurements made during the 2006 TexAQS II campaign near Houston, TX. More recently, Kaku et al.

120   (2014) showed, for a range of marine atmospheres, that the application of this spectral approach to

121   obtain FMF from three-wavelength scattering coefficient measurements was largely coherent with the

122   sub-micron fraction of scattering (SMF), obtained from scattering coefficient measurements of the fine

123   and coarse mode components using impactor-based separation of the aerosol. These studies, and

124   others, provide a useful basis for understanding the accuracy and applicability of the parameters

125 retrieved from remote sensing data. However, further assessment in a wide range of environments is

126 necessary given that networks employing such spectral remote sensing algorithms (AERONET and some

127 surface based sites) represent locations impacted by particles from diverse sources.

128 In this work, measurements of aerosol optical properties (extinction, scattering and absorption

129 coefficients) made at multiple wavelengths during the 2010 Carbonaceous Aerosols and Radiative

130 Effects Study (Fast et al., 2012; Zaveri et al., 2012) are reported and analyzed using the O'Neill et al.

131 (2003) and the O'Neill et al. (2008b) methods. The measurements were made at two locations near

132 Sacramento: a more urban site in Granite Bay, CA (T0) and a more rural site in Cool, CA (T1) that were

133 often linked by direct atmospheric transport. The multi-wavelength measurements were made using

134 three types of optical instruments (specifically seven separate instruments at the two locations). The

135 multi-wavelength measurements of the extinction coefficients (either measured directly or produced

136 from the sum of scattering and absorption coefficients) are used to retrieve the fine mode fraction of

137 extinction and fine mode effective radius. These results from the retrieval, described in more detail in

138 the next section, are compared to other, complementary *in situ* measurements. Scattering and

139 absorption coefficients were measured after aerodynamic separation into the PM_1 and PM_{10} fractions,

140 which allowed the sub-micron fraction (SMF) of extinction to be directly determined. The *in situ* SMF can

141 be compared with the FMF from the spectral retrieval method. (In this work, sub-micron particles are

142 those with nominal aerodynamic diameters ($d_{p,a}$) smaller than 1 μm, likely resulting in geometric

143 diameters below 800 nm.) Also, size distribution measurements allowed for determination of the fine-

144 mode effective radii (via Eqn. 1), which are compared with that obtained from the spectral retrieval.

Theoretical Approach

145 **Theoretical Approach**

146 *The Spectral Deconvolution Algorithm with Fine Mode Curvature (SDA-FMC) Approach*

147 This section provides a qualitative description of the fine and coarse mode AOD (or extinction)

148 deconvolution (SDA) algorithm and fine mode optical sizing (FMC or fine mode curvature) method

149 developed by O'Neill. The details of the derivation and application of the SDA are provided in previous

150 publications (O'Neill et al., 2005; Atkinson et al., 2010; Kaku et al., 2014). The MATLAB code that

151 implements the approach is available from O'Neill upon request. Application of both approaches

152 requires a robust set of measurements of aerosol optical extinction or scattering (or optical depth) at a

153 minimum of three wavelengths that should be widely spread across the optical region of the spectrum

154 (near UV through the visible to the near IR; see, for example, O'Neill et al. (2008a)).

155   The fundamental assumption of the SDA approach is that most ambient aerosol size distributions are

156   composed of two optically-relevant modes: a fine mode having an effective radius (and to a lesser

157   extent, geometric standard deviation) that is a function of atmospheric processing, and a separate

158   coarse mode, largely in the supermicron ($d_{p,a}$ > 1 µm) size range. A common assumption is that the fine

159   mode is more closely associated with anthropogenic activities and the coarse mode with natural

160   sources, although this can be somewhat confounded by smoke from biomass burning (Hamill et al.,

161   2016). The FMC (Fine Mode Curvature) algorithm employs the fine mode optical parameters retrieved

162   using the SDA to estimate both a fundamental indicator of optical particle size (the fine mode van de

163   Hulst parameter) and from this, an indicator of microphysical particle size (the fine mode effective

164   radius); these are both defined below.

165   *Spectral deconvolution of the fine and coarse mode extinction and derivation of the fine mode*

166   *spectral derivatives (SDA)*

167   The spectral deconvolution algorithm begins by isolating the fraction of total extinction due to particles

168   in the fine mode, based on the stronger dependence of the extinction (scattering)[1] on wavelength for

169   smaller particles. Current applications of the method start by fitting ln(b_{ext}) (or ln(b_{scat}) or ln(AOD))

170   versus ln(λ) to a second order polynomial, where b_{ext} is the measured wavelength-dependent extinction

171   coefficient (see Atkinson et al. (2010) and Kaku et al. (2014) for scattering and extinction coefficient

172   applications, Saha et al. (2010) for a sunphotometry AOD application and Baibakov et al. (2015) for a

173   starphotometry AOD application). The extinction and its first and second derivatives at a reference

174   wavelength of 500 nm are determined from the fit. The first derivative (i.e. slope) is denoted α in

175   analogy to the Ångström exponent, but in this non-linear, second order approach it is a function of

176   wavelength. The second derivative α′ (i.e. spectral curvature) may, in principle, be wavelength

177   dependent over the observed range, but using a second order polynomial fit yields a wavelength-

178   invariant version. Values of α and α′ associated with the fine mode and the coarse mode are indicated

179   using subscript f or c, respectively. In this work, only a second order fit is possible because only three

180   measurements are used to define the wavelength dependence. In the SDA-FMC approach, the observed

181   spectral derivative (α) is combined with the spectral derivative of the fine modes (α_f) to produce the fine

---

[1] We will stop inserting "(scattering)" at this point although all references below should be understood to apply to
both scattering and extinction.

182   mode fraction of extinction while the fine mode slope and curvature are both used in determining the

183   fine mode effective radius.

184   One reason for choosing a mid-visible reference wavelength of 500 nm for assessing curvature and

185   slopes is that the variation of the extinction for coarse mode aerosols is minimal in this spectral region

186   (O'Neill et al., 2001). The algorithm assumes constant values of the spectral slope and curvature for all

187   coarse mode aerosols at this wavelength (500 nm), specifically α_C = -0.15 and α'_C = 0.0 (with an assumed

188   uncertainty, as per O'Neill et al. (2003), of ±0.15 and ±0.15 respectively). An assumption of aerosol

189   bimodality (at least as far as measurements in the visible and near-IR are concerned) yields a series of

190   three succinct equations if the approximation level relative to a theoretical Mie representation (O'Neill

191   et al., 2001) is limited to second order in ln λ space. These three equations express the relationships

192   between the observed parameters (AOD or extinction coefficient, α, α') and their fine and coarse mode

193   analogues (O'Neill et al., 2001). A set of three equations can be then inverted to yield the fine mode

194   spectral derivative, the fine mode curvature (α_f') and the fine and coarse mode AOD or b_{ext} values. The

195   observationally determined total and fine mode spectral derivative and proscribed coarse mode spectral

196   derivative are then used to calculate the fine mode fraction of extinction at the reference wavelength

197   as:

198
$$FMF = \frac{\alpha - \alpha_c}{\alpha_f + \alpha_c} \qquad (2)$$

199

200   *Estimation of the Fine Mode Effective Radius – the Fine Mode Curvature (FMC) approach*

201   Using the spectral derivatives for the fine mode obtained from the SDA portion of the approach, an

202   estimate of the fine mode effective radius is obtained. The basis for this approach is a parameterization

203   of a strong relationship between the effective van de Hulst phase shift parameter for fine mode

204   aerosols and a polar angle representation of α_f' vs. α_f (O'Neill et al., 2005). The fundamental van de Hulst

205   parameter for the fine mode, $\rho_{eff,f}$, is given by:

206

207
$$\rho_{eff,f} = 2 * \frac{2\,\pi R_{eff,f}}{\lambda}|m - 1| \qquad (3)$$

208

209   where λ is the reference wavelength and m is the complex refractive index at that wavelength (ibid.) An

210   estimate of this purely optical parameter derived from the α_f' vs. α_f polar relationship allows extraction

211   of an effective radius for the fine mode from the SDA-obtained slope and curvature, if the refractive

212   index of the particles is known. Since the refractive index is generally unknown for the situations we

213   consider here, the information provided by this approach is actually a combination of size and

214   composition. In many cases, an average, constant value for the real portion of the refractive index can

215   be assumed and the imaginary part neglected to provide an estimate of the effective radius; this is, in

216   part, because the imaginary component is typically much smaller than the real component of the

217   refractive index, and thus the $\rho_{eff,f}$ value is relatively insensitive to variations in the imaginary

218   component. This treatment is questionable if strong changes in the average composition that lead to

219   changes in m are suspected, for example if the composition shifted from pure sulfate aerosol (m = 1.53 +

220   0i) to a brown carbon organic (m = 1.4 + 0.03i) this would introduce a 33% shift in the derived radius

221   with no change in actual size; the majority of this shift in the derived radius would result from the

222   change in the real component of the refractive index.

223   The FMC method has been less rigorously validated than the SDA portion and is expected to be more

224   susceptible to problems related to measurement errors and a decreasing sensitivity with decreasing fine

225   mode fraction of extinction. The polar-coordinate system relationship is a strong, near monotonic fit

226   based on Mie simulations over a variety of aerosol types and sizes (O'Neill et al., 2005; O'Neill et al.,

227   2008a); its validation is largely confined to comparisons with the more comprehensive AERONET

228   inversions of (Dubovik and King, 2000). These inversions, which require the combination of AOD and sky

229   radiance data, are of a significantly lower frequency than simple AOD measurements (nominally once

230   per hour versus once every 3 minutes respectively). The comparisons (for the limited data set of O'Neill

231   et al. (2005) and confirmed by more recently unpublished AERONET-wide comparisons) show averaged

232   AERONET-SDA differences of 10% $\pm$ 30% for large FMF values > 0.5.

233   Application of the SDA-FMC method to in situ extinction measurements

234   This paper seeks to address the following two key questions pertaining to the use of the SDA-FMC

235   algorithm with extinction measurements, especially those produced by the cavity ring-down

236   instruments, to extract information about aerosol size, both the partitioning of the extinction between

237   the fine and coarse modes and the extraction of a single parameter size characterization of the fine

238   mode.

1.) Can the approach be used reliably to extract the fine and coarse mode fractions of the extinction in situations where only a single optical instrument is used?

and,

2.) In situations where complementary measurements (mobility-based sizers, parallel or switching nephelometers, etc.) are available, what information can be determined from the comparison of the products of the SDA-FMC approach to comparable information obtained in other ways?

It has been suggested that a single multi-wavelength optical measurement of the fine mode fraction could be less expensive than derivation of the sub-micron fraction of scattering using parallel nephelometers (Kaku et al., 2014). The use of two size-selected inlets (e.g., 1 and 10 μm cyclones) and parallel nephelometers is not prohibitively expensive, but the typical concerns regarding calibration maintenance and careful and consistent application of correction factors for truncation angle and non-Lambertian illumination can be magnified when measurements are combined (either as differences or ratios) since systematic errors may not undergo partial cancellation like random errors.

In principle, the use of two parallel CRD extinction measurements could mitigate some of the possible errors with parallel nephelometers. Cavity ring-down measurements do not (in principle) need to be calibrated and have very small truncation errors (Smith and Atkinson, 2001; Brown, 2003). In practice, two types of "calibrations" are applied to CRD measurements: a zeroing procedure that is usually a measurement of filtered air for aerosol measurements and a cavity path length correction because the complete mirror-to-mirror distance of the optical cavity is typically not filled with aerosols (to keep the mirrors clean) (Langridge et al., 2011). The former (zeroing) limits instrument precision and sometimes accuracy while the latter (path length) limits instrument accuracy. In general these procedures are identical for the two parallel instruments and are very stable in time, so they would only be expected to produce a small and consistent bias. To our knowledge, currently no single-package, multi-wavelength direct extinction (cavity-enhanced) instruments are commercially available. Multiple single-wavelength instruments operating at different wavelengths could be deployed, but might be prohibitively expensive.

For detailed knowledge of the fine mode size distribution, the use of scanning mobility analyzer-based sizing instruments is preferable since the full mobility size distribution is obtained, as opposed to only the effective radius provided by the FMC procedure. However, scanning mobility sizer instruments typically have maximum diameters of only 700 to 800 nm, and both scanning and multi-channel variants are of comparable expense and complexity as CRD instruments. In order to obtain additional

269   information about the coarse mode size distribution and contribution to the optical effects, an aerosol

270   particle spectrometer (APS) is generally added to the measurement suite.

271   The purely spectrally-based mode separation inherent in the SDA obviates the need for a physical cut

272   point selection, such as that required to measure the PM_1 scattering product used in this work. This can

273   be advantageous, since selection and maintenance of a size cut-point is a possible source of differences

274   between some measurements (and variability of all measurements using physical separation) of the sub-

275   micron fraction (SMF) of scattering, absorption or extinction. The SMF is fundamentally different from

276   the FMF, although both provide an indication of the fractional optical contribution of smaller particles.

277   In fact, there are fundamental differences between many of the SMF or FMF data products that are

278   currently available. For example, the Dubovik and King (2000) SMF data product tries to locate the

279   separation radius (called the inflection point) at a minimum of the particle size distribution obtained

280   from the inversion procedure. This results in a variable cut point that can be interpreted as assigning a

281   portion of the coarse mode to the fine mode (O'Neill et al., 2003). The aerodynamic diameter selected

282   for the physical separation used in the SMF presented in this work might result in some mis-assignment

283   of fine mode extinction to the coarse mode, since (i) the aerodynamic separation results in a cut point

284   that is less than 1 μm geometric diameter and (ii) the cut point might not correspond to a local

285   minimum of the size distribution. These definitional differences should be kept in mind when comparing

286   fine mode apportionments (SMF or FMF) from different measurements/data treatments. And all of

287   these data products will usually differ significantly from the optical properties of the $PM_{2.5}$ fraction used

288   to define the fine mode for air quality regulations and to exclude larger particles in the CRD instruments

289   at T0. The latter allowed a significant fraction, but not all of the optically coarse particles into the

290   instruments, as shown in the Results section. For the comparisons presented in this work, in cases

291   where there is significant penetration of one of the modes into the size regime defined by the physical

292   cut-point as the other mode (or significant overlap of two or more size modes) there are noticeable

293   differences between the physically-defined SMF and the FMF produced by the SDA.

Experimental

294

295   The instrument suites used, sampling conditions and methodology and goals of the CARES study have

296   been summarized by (Zaveri et al., 2012). A summary of the instrumentation used to make the light

297   extinction, scattering and absorption measurements is provided in Table 1. Extinction was measured

298   either directly (using cavity ringdown spectroscopy) or as the sum of scattering and absorption. A brief

299   description of the key instruments used in the current analyses is given below.

300

301   **Table 1: Summary of optical instruments used at the T0 and T1 sites**

Property	Instrument	Wavelength	Size Cut[*]
		T0	
Extinction	UCD CRD	405, 532 nm	2.5 μm
	PSU CRD	1064 nm	2.5 μm
Scattering	PNNL Nephelometer	450, 550, 700 nm	1 μm, 10 μm
Absorption	PNNL PSAP	470, 522, 660 nm	1 μm, 10 μm
		T1	
Extinction	PSU CRD	355, 532, 1064 nm	None applied
Scattering	PNNL Nephelometer	450, 550, 700 nm	1 μm, 10 μm
Absorption	PNNL PSAP	470, 522, 660 nm	1 μm, 10 μm

*For the entries with two size cuts listed, the sampling system switched
between the two on a 6 minute cycle

302

303   *Instruments used at the T0 site (American River College, Granite Bay, CA USA)*

304   Cavity Ring-down Extinction: The b_{ext} measurements at 405 nm and 532 nm were made using the UC

305   Davis two-wavelength Cavity Ring Down-Photoacoustic Spectrometer (CRD-PAS) instrument (Langridge

306   et al., 2011; Lack et al., 2012). Full details of these measurements are available in Cappa et al. (2016) and

307   Atkinson et al. (2015). These measurements were only made for a subset of the CARES campaign, from

308   20:00 PDT on 16 June through 09:00 PDT on 29 June. At 532 nm, b_{ext} was measured at low (~25%), mid

309   (~75%) and high (~85%) relatively humidity. At 405 nm only low RH measurements were made, and so

310   only the low RH 532 nm measurements are used in this study. The CRD-PAS sampled behind a PM$_{2.5}$

311   (aerodynamic diameter <2.5 μm) URG Teflon-coated aluminum cyclone. A separate CRD instrument

312   deployed by the PSU group at T0 used a single optical cavity to measure the sub-2.5 μm (sampled

313   through a similar URG cyclone) aerosol extinction coefficient at 532 and 1064 nm simultaneously

314   (Radney et al., 2009). This instrument did not incorporate intentional RH control, but efforts were made

315   to maintain nearly ambient conditions, resulting in low RH (25 - 40 %) throughout most of the campaign,

316   as measured by an integrated RH/T sensor (Vaisala HMP70). Daytime ambient RH was similar to the low

317   RH value during the CARES campaign (Fast et al., 2012).

318   To obtain three-wavelength b_{ext} measurements for use in the SDA-FMC analysis, we combined the

319   measurements from the two CRD instruments. First, the 532 nm time series data were overlaid and

320   examined for differences: temporal correspondence between the data was demonstrated (except for a

321   clear difference in precision, the UCD CRD having approximately 3 times better precision than the PSU

322   instrument at comparable integration times). A scatterplot (Figure S1) between the two data sets

323   showed good correlation with a best fit line having a slope = 0.87 and an intercept that was statistically

324   indistinguishable from zero. With this assurance that the two instruments were measuring the same

325   aerosol with comparable measurement quality, the PSU 1064 nm data are used with the UCD 532 nm

326   and 405 nm low RH data for the SDA-FMC analysis.

327   Size-selected absorption and scattering (Nephelometer and PSAP): The low RH scattering and absorption

328   coefficients were alternatingly measured for PM_{10} and PM_1 aerodynamic size selected aerosol using the

329   PNNL Aerosol Monitoring System, a clone of NOAA/CMDL's Aerosol Monitoring System (detailed

330   description at http://www.esrl.noaa.gov/gmd/aero/instrumentation/instrum.html and in Zaveri et al.

331   (2012)). The relevant measurements are: light absorption coefficients at three-wavelengths (Radiance

332   Research Particle Soot Absorption Photometer [PSAP]) and total scattering coefficients (three-

333   wavelength nephelometer, TSI 3563). The absorption coefficients were adjusted to the nephelometer

334   wavelengths using an inverse wavelength dependence. The absorption and scattering coefficients for

335   PM_1 or PM_{10} are then summed after averaging to one-hour intervals and using the mean of the 450 and

336   550 nm values to obtain b_{ext}(500 nm). The extinction fraction of the PM_1 (herein, the SMF) at the visible

337   wavelength (500 nm) is then calculated from their ratio

338    $$SMF_{ext} = \frac{b_{ext,PM1}}{b_{ext,PM10}}$$ (4)

339   Particle size control was effected by 2 impactors (1 μm and 10 μm) upstream of the PSAP and

340   Nephelometer. The 10- μm impactor was always present in the sampling line, and the flow was switched

341   to run through the 1- μm impactor on 6-min intervals, yielding alternating 6-min measurements of

342   submicron and coarse (< 10 μm) particle modes.

343   Fine particle size distribution: The submicron dry particle mobility diameter ($d_{p,m}$) size distribution (12

344   nm to 737 nm) was measured using a scanning mobility particle sizer (SMPS) comprised of a charge

345   neutralizer, differential mobility analyzer and condensation particle counter (TSI 3081 DMA column and

346   model 3775 CPC). The SMPS data were corrected for multiply-charged particles and diffusional losses.

347   These size distribution measurements are used to calculate $R_{eff,f}$ values from Eqn. 1, which will be

348   referred to as $R_{eff,f,size}$. It should be noted that a mobility diameter of 737 nm corresponds to an

349   aerodynamic diameter of 919 nm (assuming a density of 1.5 g cm^{-3}, a reasonable value for the campaign

350   based on the observed particle composition (Atkinson et al., 2015)).

351

352   *Instruments used at the T1 site (Evergreen School, Cool, CA USA)*

353   Cavity Ring-down Extinction: The PSU group deployed a custom CRD instrument that used separate

354   optical cavities to measure b_{ext} at 355 nm, 532 nm, and 1064 nm simultaneously in each of four separate

355   flow systems that were intended to measure total and submicron aerosol and submicron aerosol that

356   had been conditioned to have elevated and suppressed RH. Only the total aerosol flow results are used

357   here as this prototype system suffered from signal to noise problems and RH/temperature control

358   issues. As with the T0 PSU instrument, the total aerosol system attempts to measure particle extinction

359   at nearly ambient conditions, resulting in low RH (25 – 40 %) throughout most of the campaign, as

360   measured by an integrated RH/T sensor (Vaisala HMP70). No intentional size cut was applied to these

361   measurements, although the system was not optimized for transmission of coarse mode particles.

362   Size-selected absorption and scattering (Nephelometer and PSAP): An identical instrument suite to that

363   used at T0 was deployed and the same data analysis was conducted.

364   Fine particle size distribution: The SMPS used at T1 is a similar design described in (Setyan et al., 2012)

365   and it measured low RH particle sizes from 10 nm to 858 nm. The SMPS data were corrected to take into

366   account the DMA transfer function, the bipolar charge distribution, the CPC efficiency and the internal

367   diffusion losses.(Setyan et al., 2014)

368   **Results and Discussion**

369   *Fine mode fraction of extinction*

370   The CRD-based extinction measurements were used to derive the FMF_{ext} using the SDA. This will be

371   referred to as the $FMF_{ext,CRD}$. For the T0 site, the $FMF_{ext,CRD}$ is for $PM_{2.5}$ while at T1 no physical cut point

372   was introduced, so PM_{10} is a reasonable expectation. The time series of the CRD-based b_{ext} values and of

373   the derived $FMF_{ext,CRD}$ at the T0 site are shown in Figure 1 (all times in PDT – local time during the study).

374   The $FMF_{ext,CRD}$ varies from 0.55 to 1, with a mean of 0.78 ± 0.1 (1 σ).

375

376
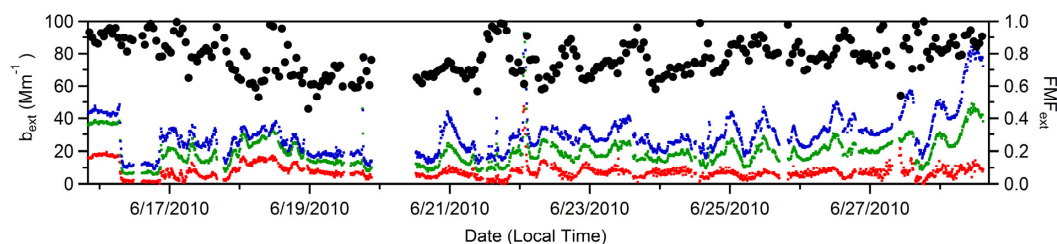
Figure 1 – Time series of CRD extinction coefficient observations (left axis) and the derived
$FMF_{ext,CRD}$ (right axis) at T0 during the time period analyzed in this work. The blue, green and red
traces are the 405 nm, 532 nm and 1064 nm b_{ext} (respectively) and the black points show the 1 h
average $FMF_{ext,CRD}$ from the SDA analysis. A $PM_{2.5}$ size cut was applied during the sampling.

381

382 The fine mode fraction of extinction at T0 was alternatively determined from the PM_{10} b_{ext}

383 measurements from the nephelometer and PSAP, referred to as $FMF_{ext,sum}$. The SDA-derived $FMF_{ext,CRD}$

384 and $FMF_{ext,sum}$ values are compared with the sub-micron fraction of extinction determined from the

385 combined PM_1 and PM_{10} nephelometer and PSAP measurements (from the latter part of the campaign)

386 at T0 (Fig. 2). The $FMF_{ext,CRD}$, $FMF_{ext,sum}$ and $SMF_{ext,sum}$ all exhibit the same general temporal dependence.

387 In general, the $FMF_{ext,CRD}$ > $FMF_{ext,sum}$ ~ $SMF_{ext,sum}$ although the specific relationships vary with time. For

388 example, there are periods when the $FMF_{ext,sum}$ and $SMF_{ext,sum}$ are nearly identical (e.g. 20 June – 23

389 June) and periods when the $SMF_{ext,sum}$ is somewhat lower than the $FMF_{ext,sum}$ (e.g. 24 June – 25 June).
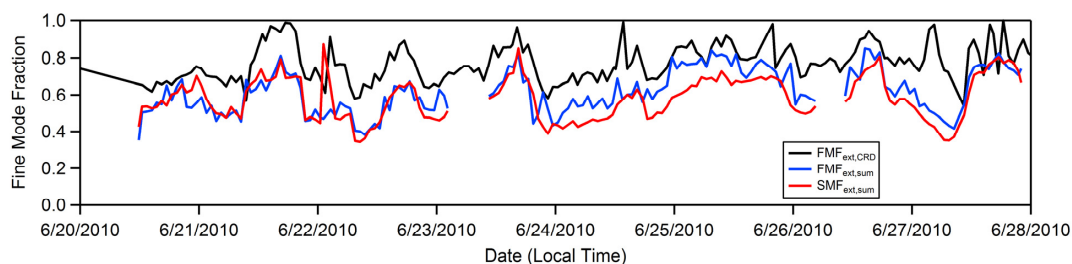
390

391 **Figure 2** – Time series of the fine mode fractions and sub-micron fraction of extinction at T0. The

392 red trace is the $SMF_{ext,sum}$ determined from the $b_{ext}(PM_1)$ / $b_{ext}(PM_{10})$ ratio. The black and blue

393 traces are the FMF_{ext} from the SDA analysis of the CRD extinction (black) and nephelometer +

394 PSAP extinction (blue). The $FMF_{ext,CRD}$ values are the same as those of Fig. 1 for the latter half of

395 the campaign.

396

397 The $FMF_{ext,CRD}$ was determined for $PM_{2.5}$ while the $FMF_{ext,sum}$ was determined for PM_{10}. If a substantial

398 fraction of the scattering was contributed by particles with diameters >2.5 µm, then the $FMF_{ext,CRD}$

399   should be larger than the $FMF_{ext,sum}$, as was observed. Kassianov et al. (2012) used measured particle size

400   distributions from CARES to show that supermicron particles contributed significantly to the total

401   scattering, consistent with the observation that $FMF_{ext,CRD} > FMF_{ext,sum}$. Variability in the difference

402   between the $FMF_{ext,CRD}$ and $FMF_{ext,sum}$ likely reflects variability in the contribution of these larger particles

403   to the total scattering.

404   The $FMF_{ext,CRD}$, $FMF_{ext,sum}$ and $SMF_{ext,sum}$ were similarly determined from the measurements at the T1 site

405   (Figure 3). For T1, the CRD measurements were made for particles without any intentional size cut

406   applied, as opposed to the $PM_{2.5}$ size cut used for the T0 measurements. At this downwind site the

407    $SMF_{ext,sum}$, $FMF_{ext,CRD}$ and $FMF_{ext,sum}$ were all very similar, both in terms of the absolute magnitude and

408   the temporal variability. The $FMF_{ext,CRD}$ ranged from 0.3 to 0.85, with a mean of 0.66 ± 0.19. That the

409    $FMF_{ext,CRD}$ and $FMF_{ext,sum}$ are very similar in absolute magnitude for T1 but differ at T0 (while still

410   exhibiting similar temporal variability) is likely related to the application of an intentional size cut for the

411   CRD measurements at T0 but not at T1. The observations suggest that the T1 CRD without the size cut

412   samples coarse-mode particles with a similar efficiency as the nephelometer and PSAP having the PM_{10}

413   size cut.

414   Overall, these results indicate that the use of the spectral deconvolution algorithm on optical data can

415   robustly provide information on the fine mode fraction of extinction. Moreover, since the FMF_{ext} results

416   at T1 are similar for the two types of extinction measurements, it seems that the narrower wavelength

417   range of the nephelometer (450, 550, 700 nm) and PSAP (470, 522, 660 nm) compared to the CRD

418   instruments used here is still adequate to define the spectral dependence of extinction for extraction of

419   the slope and curvature parameters. However, the differences observed at both sites highlight the fact

420   that there is not a precise definition of "fine" and "coarse" in terms of a specific size cut in the optical

421   method. The effective size cut is dependent on the shapes of the size distributions in the "fine" and

422   "coarse" size regimes and the extent of overlap between them, which is dependent on the size range of

423   particles sampled (e.g. $PM_{2.5}$ versus PM_{10}). Nonetheless, since the major sources of fine and coarse

424   mode particles are likely to be reasonably distinct in many environments, the $FMF_{ext,CRD}$ can provide a

425   characterization of the variability in the contributions of such sources to the total scattering.

426

427

428
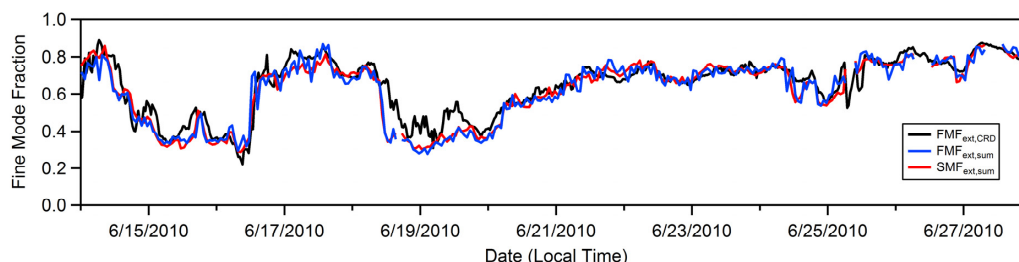
429

430   **Figure 3** – the fine mode fraction of extinction (SMF and FMF_{ext}) for the latter half of the

431   campaign at T1. Here, the $FMF_{ext,CRD}$ is determined for particles sampled without a size cut

432   applied.

433

434   *Effective fine mode radius product of SDA-FMC*

435   The SDA-FMC analysis also allows for derivation of the fine mode effective radius, $R_{eff,f}$, via Eq. 3.

436   Determination of $R_{eff,f}$ requires knowledge of the real and imaginary parts of the refractive index. Here,

437   an average value of $m_r = 1.55$ is used, based on Atkinson et al. (2015), and absorption is assumed to be

438   negligible. The latter is a reasonable assumption given the relatively high single scatter albedo values at

439   the two sites (Cappa et al., 2016), and because assuming the particles to be slightly absorbing has

440   minimal influence on the results. Values of $R_{eff,f}$ are determined using both the CRD-measured b_{ext} and

441   the PM_{10} b_{ext} from the nephelometer + PSAP measurements for both T0 and T1 (Figure 4). $R_{eff,f}$ values

442   are also determined from the PM_1 nephelometer + PSAP measurements at both sites. Comparison of the

443    $R_{eff,f}$ values between the PM_{10} and PM_1 measurements provides a test of the robustness of the overall

444   retrieval method. The $R_{eff,f}$ from the CRD measurements will be referred to as $R_{eff,f,CRD}$ and from the

445   nephelometer + PSAP as $R_{eff,f,sum}$. Comparator values of $R_{eff,f}$ were also calculated from the observed

446   mobility size distributions using Eqn. 1, and are referred to as $R_{eff,f,size}$.

447

448
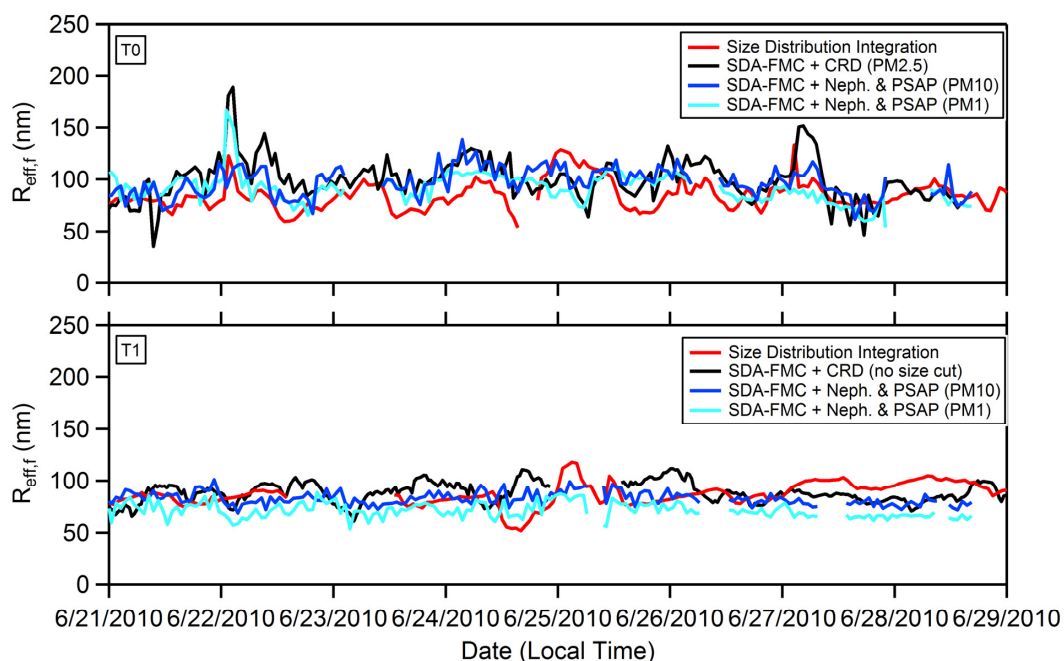
Figure 4 – Time series of the effective fine mode radii, $R_{eff,f}$, produced by the SDA-FMC analysis of the
CRD data (black) and the nephelometer + PSAP data (blue) from T0 (top) and T1 (bottom). For the
nephelometer + PSAP observations, separate results are shown using either the PM_{10} (dark blue) or
PM_1 (light blue) observations. The $R_{eff,f}$ values determined from the size distribution measurements (i.e.
from Eqn. 1) are shown in red.

454

The SDA-FMC-derived $R_{eff,f}$ values from the CRD and from the nephelometer + PSAP exhibit reasonably

good agreement in terms of the absolute values and the temporal variability at both the T0 and T1 sites

(Table 2, Fig. 4). Notably, there is good agreement between the $R_{eff,f,sum}$ values obtained from the PM_{10}

and PM_1 measurements. This provides an important validation of the SDA-FMC procedure, since the

coarse mode contribution to the PM_{10} extinction is substantial and highly variable (Figure 2 and Figure

3).

At T0, the derived $R_{eff,f}$ values range from approximately 70 nm to 140 nm (Table 2), with a few short-

duration periods when $R_{eff,f}$ is outside this range, reflecting short-duration variability in the particle

sources. At T1 the derived $R_{eff,f}$ are generally less variable, ranging from approximately 65 nm to 110 nm,

with fewer particularly low or high periods. The mean $R_{eff,f}$ values between the two sites are similar

(Table 2). At T0, there is a fair degree of temporal coherence of the SDA-FMC results and those obtained

466   from integration of the size distributions. The generally good temporal agreement between the

467   optically- and size-derived $R_{eff,f}$ values are even observed during periods where the changes in radius

468   happened rapidly, for example near midnight between June 21-22. On that night there is some evidence

469   that paving operations near the T0 site produced a strong local source of asphalt particles in the coarse

470   mode with a long tail into the sub-micron regime (Zaveri et al., 2012; Cappa et al., 2016). This short-

471   duration source of large particles pushed the $R_{eff,f}$ temporarily towards larger values. (The $R_{eff,f}$ changes

472   from the nephelometer + PSAP at this time were smaller than from the CRD or size distribution

473   observations. Most likely this reflects the alternating 6-min sampling of the nephelometer and the very

474   short duration of the event leading to discrepancies in the 1 h average.)

475   Despite the generally good correspondence between $R_{eff,f,size}$ and the optically derived values, the $R_{eff,f,size}$

476   values were often (but not always) smaller (Table 2). This is most clearly seen when comparing the

477   average diurnal profiles of the $R_{eff,f}$ values from the different methods, as shown in Figure 5. All three

478    $R_{eff,f}$ estimates exhibit similar diurnal behavior at T0, even though the $R_{eff,f}$ from the SDA-FMC method

479   are larger than $R_{eff,f,size}$. The diurnal variability in the $R_{eff,f}$ is more pronounced at T0 than at T1. The

480   diurnal trend in the effective radius of the fine mode at T0 from all methods exhibits a minimum at

481   around mid-day and then an increase to a maximum right near daybreak. Particle number and sizes at

482   both sites were influenced by frequent regional new particle formation and growth events during CARES

483   (see Figure S2). The events tended to start in the morning with a sharp increase of 10 - 20 nm particles

484   followed by growth of these particles to $50 - 100$ nm in the afternoon as discussed in Setyan et al.

485   (2014). The next day the cycle repeats (on average) with the introduction of the new small particles

486   which has the effect of decreasing the average particle radius (Setyan et al., 2014). Although observed at

487   both sites, the new particle formation events had a greater impact on the size distributions at T0,

488   especially in terms of surface area-weighted size distributions that determine $R_{eff,f}$. In part, this is likely

489   because of continued growth of the new particle mode as it transits from T0 to T1.

490

491
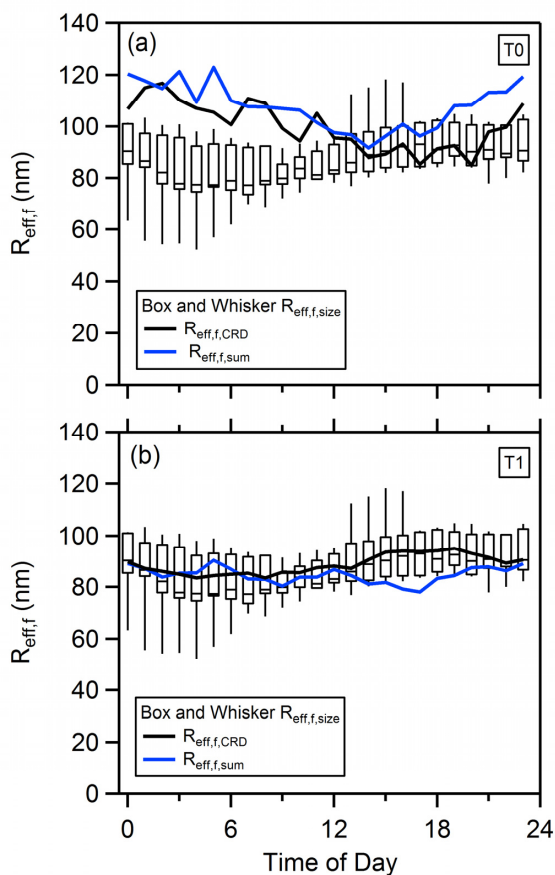
Figure 5 – The diurnal dependence of $R_{eff,f}$ for the period shown in Fig. 4 for the (a) T0 and (b) T1
sites. The box and whisker plot (bottom and top of box are 5% and 95% of data range, bar is
mean, and whiskers extend to full range) shows the results from the direct size distribution
measurement ($R_{eff,f,size}$), while the lines show the mean diurnal dependence of the optically
derived $R_{eff,f}$, using the CRD (black) and nephelometer + PSAP (blue) measurements.

497

498   One possible explanation for the differences between the optically and size-derived $R_{eff,f}$, in particular at

499   T0, may be inaccurate specification of the refractive index. Temporal variations in or an overall offset of

500   the real refractive index used here from the true value would lead to errors in the optically derived $R_{eff,f}$.

501   The refractive index is used to convert the derived van de Hulst parameter to $R_{eff,f}$ (Eqn. 3). Given the

502   form of the relationship, an absolute error in the real RI of 0.1—likely an upper limit—corresponds to an

503   error in the derived $R_{eff,f}$ of 20%, with larger values of the real RI leading to smaller derived $R_{eff,f}$. The

504   imaginary component was assumed zero. The effective imaginary RI is likely ≤ 0.01, given the range of

505 single scatter albedo values observed (Cappa et al., 2016). Thus, the assumption of zero for the

506 imaginary RI introduces negligible error. The actual real RI depends on the particle composition since

507 different chemical components (e.g. sulfate, organics, dust) have different RI values. Here, the RI values

508 used were determined based only on measurements of the non-refractory PM composition and only an

509 average value was used (Atkinson et al., 2015). To the extent that refractory components, in particular

510 dust or sea salt, contributed to the fine mode scattering, their influence on the real RI would not be

511 accounted for. However, dust and sea salt contributions are most likely confined primarily to the coarse

512 mode. Thus, the fine mode real refractive index is unlikely to be strongly affected by their presence and

513 the real RI can probably be constrained to a fairly narrow range around 1.5. The relative uncertainty of

514 the $R_{eff,f}$ derived from the SDA-FMC method has been estimated as ranging from 40% to 70%. This range

515 of values was computed from a quadrature combination of the estimated errors (20-50%) in the SDA-

516 FMC retrieval (O'Neill et al., 2003), the CRD measurements (< 5% for the UCD and T0 PSU instrument

517 and 20% for the T1 PSU instrument) and the refractive index term above (estimated maximum of 20%).

518 In this context, the agreement shown in Fig. 4 is acceptable and may suggest that the above error

519 estimates are overly conservative.

520 **Table 2**: Summary statistics for $R_{eff,f}$ values (nm)

Site	Method	Maximum (nm)	Minimum (nm)	Mean (nm)	Standard Deviation (nm)
T0	SDA-FMC + CRD (PM$_{2.5}$)	189	35	100	21
T0	SDA-FMC + Neph. & PSAP (PM$_{10}$)	139	62	97	14
T0	Size Distribution Integration	133	54	85	14
T1	SDA-FMC + CRD (no size cut)	160	42	93	18
T1	SDA-FMC + Neph. & PSAP (PM$_{10}$)	101	69	83	6
T1	Size Distribution Integration	118	52	88	11

521 ## Conclusions

522 This work demonstrates that the use of a non-size-selected, three wavelength CRD measurement in

523 continuous field monitoring, coupled with the SDA-FMC analysis, can provide information about the

524 relative contribution of the fine mode to the observed total particle extinction. The retrieved value of

525 the fine mode fraction of extinction is dependent upon the size range of particles sampled and the

526 overall nature of the particle size distribution. The relationship between the FMF$_{ext}$ and the SMF$_{ext}$,

527 determined from near-coincident measurement of extinction by PM$_1$ and PM$_{10}$, provides insights into

528 the effective FMF$_{ext}$ split size. For one of the sites considered here the split point size is around 1 μm

529 while for the other it is somewhat larger than 1 μm and perhaps more variable. In many environments,

530   variability in aerosol properties on short (<10 min) timescales is relatively minimal. In such cases, a single

531   instrument can be used to sequentially sample PM_1 and PM_{10}, allowing for *in situ* measurement of both

532   the FMF_{ext} and SMF_{ext}. However, remote sensing measurements characterize only the FMF_{ext}, (or at best,

533   an optically influenced size cut as is done in the AERONET retrievals of Dubovik & King, 2000). Thus,

534   further consideration of *in situ* measurement results, such as those investigated in this study, can

535   provide insights into the interpretation of the FMF_{ext} determined from remote sensing in different

536   environments.

537   The SDA-FMC approach also allows for determination of the effective fine mode radius. The $R_{eff,f}$

538   characterizes the surface-area weighted size of the particles within the fine mode distribution The

539   similarity of the results in Figure 4 for application of the SDA-FMC to both size-selected and non-size-

540   selected aerosol as well as the comparison with results derived from the PSD measurements verify that

541   "whole air" measurements (i.e., no imposed size-selection) can provide reliable fine mode radii at least

542   for large FMF values.

Acknowledgements

544   This work was supported by the Atmospheric System Research (ASR) program sponsored by the US

545   Department of Energy (DOE), Office of Biological and Environmental Research (OBER), including Grant

546   No. DE-SC0008937. Funding for data collection was provided by the US DOE's Atmospheric Radiation

547   Measurement (ARM) Program. All data used in this study are available from the ARM data archive at:

548   http://www.arm.gov/campaigns/aaf2009carbonaerosol. The views expressed in this document are

549   solely those of the authors and the funding agencies do not endorse any products or commercial

550   services mentioned in this publication.

Appendix A – Glossary of Symbols and Acronyms used

551

552   å   Ångström exponent (from wavelength pair)

553   α Spectral derivative of optical property

554   α' Curvature (second derivative of optical property in log-log space)

555   α_f or α'_f Fine mode version of properties (also coarse mode properties α_c)

556   AOD   Aerosol optical depth

557   b_{ext}, b_{scat}, b_{abs} Optical coefficient for extinction, scattering, absorption (inverse length units)

558   CRD   Cavity ring down

559    $R_{eff,s}$ Effective radius for fine mode

560   FMF (aka η)   Fine mode fraction of an optical property, usually extinction

561   SMF   Sub-micron fraction (particle mode with radius or diameter smaller than 1 μm)

562   ρ_f fine mode van de Hulst parameter (product of refractive index and effective radius)

563   SDA   Spectral Deconvolution Algorithm

564   FMC   Fine Mode Curvature approach

565   PM_1 Particulate matter with diameter (or radius) smaller than 1 μm (also $PM_{2.5}$, PM_{10})

566   PSAP   Particle soot absorption photometer instrument

567

References:

Anderson, T. L., Charlson, R. J., Bellouin, N., Boucher, O., Chin, M., Christopher, S. A., Haywood, J., Kaufman, Y. J., Kinne, S., Ogren, J. A., Remer, L. A., Takemura, T., Tanre, D., Torres, O., Trepte, C. R., Wielicki, B. A., Winker, D. M., and Yu, H. B.: An "A-Train" strategy for quantifying direct climate forcing by anthropogenic aerosols, B. Am. Meteorol. Soc., 86, 1795-1805, doi:10.1175/Bams-86-12-1795, 2005.

Andrews, E., Sheridan, P. J., Ogren, J. A., and Ferrare, R.: In situ aerosol profiles over the Southern Great Plains cloud and radiation test bed site: 1. Aerosol optical properties, J. Geophys. Res.-Atmos., 109, D06208, doi:10.1029/2003jd004025, 2004.

Ångström, A.: On the atmospheric transmission of sun radiation and on dust in the air, Geografika Ann., 11, 156-166, doi:10.2307/519399, 1929.

Atkinson, D. B., Massoli, P., O'Neill, N. T., Quinn, P. K., Brooks, S. D., and Lefer, B.: Comparison of in situ and columnar aerosol spectral measurements during TexAQS-GoMACCS 2006: testing parameterizations for estimating aerosol fine mode properties, Atmos. Chem. Phys., 10, 51-61, doi:10.5194/acp-10-51-2010, 2010.

Atkinson, D. B., Radney, J. G., Lum, J., Kolesar, K. R., Cziczo, D. J., Pekour, M. S., Zhang, Q., Setyan, A., Zelenyuk, A., and Cappa, C. D.: Aerosol optical hygroscopicity measurements during the 2010 CARES campaign, Atmos. Chem. Phys., 15, 4045-4061, doi:10.5194/acp-15-4045-2015, 2015.

Baibakov, K., O'Neill, N. T., Ivanescu, L., Duck, T. J., Perro, C., Herber, A., Schulz, K. H., and Schrems, O.: Synchronous polar winter starphotometry and lidar measurements at a High Arctic station, Atmos. Meas. Techniq., 8, 3789-3809, doi:10.5194/amt-8-3789-2015, 2015.

Bokoye, A. I., Royer, A., O'Neill, N. T., Cliche, P., Fedosejevs, G., Teillet, P. M., and McArthur, L. J. B.: Characterization of atmospheric aerosols across Canada from a ground-based sunphotometer network: AEROCAN, Atmosphere-Ocean, 39, 429-456, doi:10.1080/07055900.2001.9649687, 2001.

Bond, T. C., Zarzycki, C., Flanner, M. G., and Koch, D. M.: Quantifying immediate radiative forcing by black carbon and organic matter with the Specific Forcing Pulse, Atmos. Chem. Phys., 11, 1505-1525, doi:10.5194/acp-11-1505-2011, 2011.

Brown, S. S.: Absorption Spectroscopy in High-Finesse Cavities for Atmospheric Studies, Chemical Reviews, 103, 5219-5238, doi:10.1021/cr020645c, 2003.

Cappa, C. D., Kolesar, K. R., Zhang, X. L., Atkinson, D. B., Pekour, M. S., Zaveri, R. A., Zelenyuk, A., and Zhang, Q.: Understanding the optical properties of ambient sub- and supermicron particulate matter: results from the CARES 2010 field study in northern California, Atmos. Chem. Phys., 16, 6511-6535, doi:10.5194/acp-16-6511-2016, 2016.

Charlson, R. J., Valero, F. P. J., and Seinfeld, J. H.: In search of balance, Science, 308, 806-807, doi:10.1126/science.1108162, 2005.

Clarke, A. and Kapustin, V.: Hemispheric Aerosol Vertical Profiles: Anthropogenic Impacts on Optical Depth and Cloud Nuclei, Science, 329, 1488-1492, doi:10.1126/science.1188838, 2010.

604   Coen, M. C., Andrews, E., Asmi, A., Baltensperger, U., Bukowiecki, N., Day, D., Fiebig, M., Fjaeraa, A. M.,
605   Flentje, H., Hyvarinen, A., Jefferson, A., Jennings, S. G., Kouvarakis, G., Lihavainen, H., Myhre, C. L.,
606   Malm, W. C., Mihapopoulos, N., Molenar, J. V., O'Dowd, C., Ogren, J. A., Schichtel, B. A., Sheridan, P.,
607   Virkkula, A., Weingartner, E., Weller, R., and Laj, P.: Aerosol decadal trends - Part 1: In-situ optical
608   measurements at GAW and IMPROVE stations, Atmos. Chem. Phys., 13, 869-894, doi:10.5194/acp-13-
609   869-2013, 2013.

610   Doran, J. C., Barnard, J. C., Arnott, W. P., Cary, R., Coulter, R., Fast, J. D., Kassianov, E. I., Kleinman, L.,
611   Laulainen, N. S., Martin, T., Paredes-Miranda, G., Pekour, M. S., Shaw, W. J., Smith, D. F., Springston, S.
612   R., and Yu, X. Y.: The T1-T2 study: evolution of aerosol properties downwind of Mexico City, Atmos.
613   Chem. Phys., 7, 1585-1598, doi:10.5194/acp-7-1585-2007, 2007.

614   Dubovik, O. and King, M. D.: A flexible inversion algorithm for retrieval of aerosol optical properties from
615   Sun and sky radiance measurements, J. Geophys. Res.-Atmos., 105, 20673-20696,
616   doi:10.1029/2000jd900282, 2000.

617   Eck, T. F., Holben, B. N., Reid, J. S., Sinyuk, A., Dubovik, O., Smirnov, A., Giles, D., O'Neill, N. T., Tsay, S. C.,
618   Ji, Q., Al Mandoos, A., Khan, M. R., Reid, E. A., Schafer, J. S., Sorokine, M., Newcomb, W., and Slutsker, I.:
619   Spatial and temporal variability of column-integrated aerosol optical properties in the southern Arabian
620   Gulf and United Arab Emirates in summer, J. Geophys. Res.-Atmos., 113, D01204,
621   doi:10.1029/2007jd008944, 2008.

622   Fast, J. D., Gustafson, W. I., Berg, L. K., Shaw, W. J., Pekour, M., Shrivastava, M., Barnard, J. C., Ferrare, R.
623   A., Hostetler, C. A., Hair, J. A., Erickson, M., Jobson, B. T., Flowers, B., Dubey, M. K., Springston, S., Pierce,
624   R. B., Dolislager, L., Pederson, J., and Zaveri, R. A.: Transport and mixing patterns over Central California
625   during the carbonaceous aerosol and radiative effects study (CARES), Atmos. Chem. Phys., 12, 1759-
626   1783, doi:10.5194/acp-12-1759-2012, 2012.

627   George, I. J. and Abbatt, J. P. D.: Heterogeneous oxidation of atmospheric aerosol particles by gas-phase
628   radicals, Nature Chemistry, 2, 713-722, 2010.

629   Hamill, P., Giordano, M., Ward, C., Giles, D., and Holben, B.: An AERONET-based aerosol classification
630   using the Mahalanobis distance, Atmos. Environ., 140, 213-233, doi:10.1016/j.atmosenv.2016.06.002,
631   2016.

632   Hansen, J. E. and Travis, L. D.: Light-Scattering in Planetary Atmospheres, Space Sci. Rev., 16, 527-610,
633   doi:10.1007/Bf00168069, 1974.

634   Holben, B. N., Eck, T. F., Slutsker, I., Tanre, D., Buis, J. P., Setzer, A., Vermote, E., Reagan, J. A., Kaufman,
635   Y. J., Nakajima, T., Lavenu, F., Jankowiak, I., and Smirnov, A.: AERONET - A federated instrument network
636   and data archive for aerosol characterization, Remote Sens. Environ., 66, 1-16, doi:10.1016/S0034-
637   4257(98)00031-5, 1998.

638   IPCC: Climate Change 2013: The Physical Science Basis. Contribution of Working Group I to the Fifth
639   Assessment Report of the Intergovernmental Panel on Climate Change, Cambridge University Press,
640   Cambridge, United Kingdom and New York, NY, USA, 2013.

641   Kaku, K. C., Reid, J. S., O'Neill, N. T., Quinn, P. K., Coffman, D. J., and Eck, T. F.: Verification and
642   application of the extended spectral deconvolution algorithm (SDA plus) methodology to estimate

643   aerosol fine and coarse mode extinction coefficients in the marine boundary layer, Atmos. Meas.
644   Techniq., 7, 3399-3412, doi:10.5194/amt-7-3399-2014, 2014.

645   Lack, D. A. and Cappa, C. D.: Impact of brown and clear carbon on light absorption enhancement, single
646   scatter albedo and absorption wavelength dependence of black carbon, Atmos. Chem. Phys., 10, 4207-
647   4220, doi:10.5194/acp-10-4207-2010, 2010.

648   Lack, D. A., Richardson, M. S., Law, D., Langridge, J. M., Cappa, C. D., McLaughlin, R. J., and Murphy, D.
649   M.: Aircraft Instrument for Comprehensive Characterization of Aerosol Optical Properties, Part 2: Black
650   and Brown Carbon Absorption and Absorption Enhancement Measured with Photo Acoustic
651   Spectroscopy, Aerosol Science and Technology, 46, 555-568, doi:10.1080/02786826.2011.645955, 2012.

652   Langridge, J. M., Richardson, M. S., Lack, D., Law, D., and Murphy, D. M.: Aircraft Instrument for
653   Comprehensive Characterization of Aerosol Optical Properties, Part I: Wavelength-Dependent Optical
654   Extinction and Its Relative Humidity Dependence Measured Using Cavity Ringdown Spectroscopy,
655   Aerosol Science and Technology, 45, 1305-1318, doi:10.1080/02786826.2011.592745, 2011.

656   Massoli, P., Bates, T. S., Quinn, P. K., Lack, D. A., Baynard, T., Lerner, B. M., Tucker, S. C., Brioude, J.,
657   Stohl, A., and Williams, E. J.: Aerosol optical and hygroscopic properties during TexAQS-GoMACCS 2006
658   and their impact on aerosol direct radiative forcing, J. Geophys. Res.-Atmos., 114, D00f07,
659   doi:10.1029/2008jd011604, 2009.

660   Moosmuller, H., Chakrabarty, R. K., and Arnott, W. P.: Aerosol light absorption and its measurement: A
661   review, J Quant. Spec. Rad. Trans., 110, 844-878, doi:10.1016/j.jqsrt.2009.02.035, 2009.

662   O'Neill, N. T., Eck, T. F., Holben, B. N., Smirnov, A., Dubovik, O., and Royer, A.: Bimodal size distribution
663   influences on the variation of Angstrom derivatives in spectral and optical depth space, J. Geophys. Res.-
664   Atmos., 106, 9787-9806, doi:10.1029/2000jd900245, 2001.

665   O'Neill, N. T., Eck, T. F., Reid, J. S., Smirnov, A., and Pancrati, O.: Coarse mode optical information
666   retrievable using ultraviolet to short-wave infrared sun photometry: Application to United Arab Emirates
667   unified aerosol experiment data, J. Geophys. Res.-Atmos., 113, D05212, doi:10.1029/2007jd009052,
668   2008a.

669   O'Neill, N. T., Eck, T. F., Smirnov, A., Holben, B. N., and Thulasiraman, S.: Spectral discrimination of
670   coarse and fine mode optical depth, J. Geophys. Res.-Atmos., 108, 4559, doi:10.1029/2002jd002975,
671   2003.

672   O'Neill, N. T., Thulasiraman, S., Eck, T. F., and Reid, J. S.: Correction to the effective radius expression in
673   O'Neil et al. (2005), J. Geophys. Res.-Atmos., 113, D24203, doi:10.1029/2008JD011334, 2008b.

674   O'Neill, N. T., Thulasiraman, S., Eck, T. F., and Reid, J. S.: Robust optical features of fine mode size
675   distributions: Application to the Quebec smoke event of 2002, J. Geophys. Res.-Atmos., 110, D11207,
676   doi:10.1029/2004jd005157, 2005.

677   Radney, J. G., Bazargan, M. H., Wright, M. E., and Atkinson, D. B.: Laboratory Validation of Aerosol
678   Extinction Coefficient Measurements by a Field-Deployable Pulsed Cavity Ring-Down Transmissometer,
679   Aerosol Science and Technology, 43, 71-80, doi:10.1080/02786820802482536, 2009.

680   Saha, A., O'Neill, N. T., Eloranta, E., Stone, R. S., Eck, T. F., Zidane, S., Daou, D., Lupu, A., Lesins, G.,
681   Shiobara, M., and McArthur, L. J. B.: Pan-Arctic sunphotometry during the ARCTAS-A campaign of April
682   2008, Geophys. Res. Lett., 37, L05803, doi:10.1029/2009gl041375, 2010.

683   Setyan, A., Song, C., Merkel, M., Knighton, W. B., Onasch, T. B., Canagaratna, M. R., Worsnop, D. R.,
684   Wiedensohler, A., Shilling, J. E., and Zhang, Q.: Chemistry of new particle growth in mixed urban and
685   biogenic emissions - insights from CARES, Atmos. Chem. Phys., 14, 6477-6494, doi:10.5194/acp-14-6477-
686   2014, 2014.

687   Setyan, A., Zhang, Q., Merkel, M., Knighton, W. B., Sun, Y., Song, C., Shilling, J. E., Onasch, T. B., Herndon,
688   S. C., Worsnop, D. R., Fast, J. D., Zaveri, R. A., Berg, L. K., Wiedensohler, A., Flowers, B. A., Dubey, M. K.,
689   and Subramanian, R.: Characterization of submicron particles influenced by mixed biogenic and
690   anthropogenic emissions using high-resolution aerosol mass spectrometry: results from CARES, Atmos.
691   Chem. Phys., 12, 8131-8156, doi:10.5194/acp-12-8131-2012, 2012.

692   Smith, J. D. and Atkinson, D. B.: A portable pulsed cavity ring-down transmissometer for measurement
693   of the optical extinction of the atmospheric aerosol, Analyst, 126, 1216-1220, doi:10.1039/B101491,
694   2001.

695   Zaveri, R. A., Shaw, W. J., Cziczo, D. J., Schmid, B., Ferrare, R. A., Alexander, M. L., Alexandrov, M.,
696   Alvarez, R. J., Arnott, W. P., Atkinson, D. B., Baidar, S., Banta, R. M., Barnard, J. C., Beranek, J., Berg, L. K.,
697   Brechtel, F., Brewer, W. A., Cahill, J. F., Cairns, B., Cappa, C. D., Chand, D., China, S., Comstock, J. M.,
698   Dubey, M. K., Easter, R. C., Erickson, M. H., Fast, J. D., Floerchinger, C., Flowers, B. A., Fortner, E.,
699   Gaffney, J. S., Gilles, M. K., Gorkowski, K., Gustafson, W. I., Gyawali, M., Hair, J., Hardesty, R. M.,
700   Harworth, J. W., Herndon, S., Hiranuma, N., Hostetler, C., Hubbe, J. M., Jayne, J. T., Jeong, H., Jobson, B.
701   T., Kassianov, E. I., Kleinman, L. I., Kluzek, C., Knighton, B., Kolesar, K. R., Kuang, C., Kubatova, A.,
702   Langford, A. O., Laskin, A., Laulainen, N., Marchbanks, R. D., Mazzoleni, C., Mei, F., Moffet, R. C., Nelson,
703   D., Obland, M. D., Oetjen, H., Onasch, T. B., Ortega, I., Ottaviani, M., Pekour, M., Prather, K. A., Radney,
704   J. G., Rogers, R. R., Sandberg, S. P., Sedlacek, A., Senff, C. J., Senum, G., Setyan, A., Shilling, J. E.,
705   Shrivastava, M., Song, C., Springston, S. R., Subramanian, R., Suski, K., Tomlinson, J., Volkamer, R.,
706   Wallace, H. W., Wang, J., Weickmann, A. M., Worsnop, D. R., Yu, X. Y., Zelenyuk, A., and Zhang, Q.:
707   Overview of the 2010 Carbonaceous Aerosols and Radiative Effects Study (CARES), Atmos. Chem. Phys.,
708   12, 7647-7687, doi:10.5194/acp-12-7647-2012, 2012.

709

710